Supporting Information

High-rate Rare-earth based High-entropy Co-free High-Ni Cathodes for High-Performance Lithium-ion Batteries

*Yang Liu, Yan Xin, Bijiao He, Fang Zhang, Wenbo Liu, and Huajun Tian**

Y. Liu, Y. Xin, B. He, F. Zhang, W. Liu, H. Tian
Beijing Laboratory of New Energy Storage Technology and Key Laboratory of Power Station Energy Transfer Conversion and System of Ministry of Education, School of Energy Power and Mechanical Engineering,
North China Electric Power University, Beijing, 102206, China
E-mail: Huajun.Tian@ncepu.edu.cn

Experimental

Material Synthesis

The $LiNi_{0.9}Mn_{0.1}O_2$ (NM90), $LiNi_{0.9}Mn_{0.02}Al_{0.02}Mg_{0.02}Ti_{0.02}Lu_{0.02}O_2$ (HE-Lu), $LiNi_{0.9}Mn_{0.02}Al_{0.02}Mg_{0.02}Lu_{0.02}Si_{0.02}O_2$(HE-Lu1), $LiNi_{0.9}Mn_{0.02}Al_{0.02}Lu_{0.02}Ti_{0.02}Si_{0.02}O_2$ (HE-Lu2), $LiNi_{0.9}Mn_{0.02}Lu_{0.02}Mg_{0.02}Ti_{0.02}Si_{0.02}O_2$ (HE-Lu3) cathode is prepared by spray drying and one-step calcination process. First, stoichiometric amounts of Ni $(OH)_2$, MnO_2, Al_2O_3, MgO, TiO_2, SiO_2, Lu_2O_3 and LiOH were ball-milled in ethanol for 12 hours. The slurry was then transferred to a rotary evaporator and dried at 100 °C to obtain a gray precursor. The precursor was transferred to a muffle furnace and annealed at 450 °C for 5 hours. The obtained precursor was then transferred to a ball milling tank, and deionized water and 2 wt% Polyethylene glycol (PEG) and 1 wt% Hexadecyltrimethylammonium bromide (CTAB) were added as a binder and dispersant, with a mass ratio of precursor to deionized water of 2:5. After ball milling for 12 hours, a prepared slurry was obtained. The prepared slurry was pumped into a two-fluid spray dryer with an inlet temperature of 160 °C and an atomizing pressure of 0.12 MPa. Shaped spherical-like precursors could be collected at the outlet. Finally, the shaped precursors were annealed in an oxygen flow at 730 °C for 12 hours to obtain cathodes.

Material Characterizations

The chemical compositions of all cathodes were determined by ICP-OES analysis. The X-ray diffraction with a Cu Kα radiation (λ = 1.54056 Å) was performed to characterize the crystalline structures of all samples. The XRD data was collected in the scan range (2θ) of 10º-80º with a step size of 0.02º and a scan rate of 5 º/min. The obtained XRD spectra were analyzed by using the FullProf software. Microstructures of all cathodes were analyzed by scanning electron microscopy (SEM) and transmission electron microscopy (TEM). Surface compositions and elemental valence states of materials were investigated by X-ray photoelectron spectroscopy (XPS). In addition, the Ar-ion etching was implemented to obtain depth-dependent valence information and elemental distribution from samples. Cycled samples were washed three times with dimethyl carbonate (DMC) to remove the residue electrolyte salts before measurements.

Electrochemical Tests

CR2032 cells were fabricated for electrochemical evaluation. The active material (80 wt%) and carbon black (10 wt%) were thoroughly ground in a mortar, and the mixture was then added to a poly(vinylidene fluoride) (PVDF)-Nmethyl-1,2-pyrrolidone (NMP)solution with a mass fraction of 20 wt% and an appropriate amount of NMP to adjust the viscosity of the slurry. Subsequently, the slurry was doctor-bladed onto an Al foil and dried at 120 °C for 12 hours, followed by punching into 12 mm diameter discs. The mass loading of the active material in the electrodes was 1.5-2.5 mg cm^{-2}. The electrolyte consisted of a 1.2 M $LiPF_6$ solution in a mixture of ethylene carbonate (EC) and ethyl methyl carbonate (EMC) (volume ratio of 3:7) with 2.0 % VC. Lithium metal was used as the anode. The cells were assembled in an Ar-filled glove box with O_2 and H_2O levels below 0.1 ppm. For full-cells, graphite (80 wt%) was mixed with 10 wt% carbon black and 10 wt% PVDF in NMP, and the resulting slurry was cast on copper foil and then vacuum-dried at 120 °C for 12 hours, followed by punching into 14 mm diameter discs. 35 μL of electrolyte was added to each of the cathode and anode sides, and the N/P was controlled in the range of 1.15:1-1.2:1. The active mass loading of the full cells is in the range of 2-3 mg cm^{-2}. Charge-discharge tests were performed for three cycles at room temperature at 0.2 C (1C = 180 mAh g^{-1}), followed by cycling stability evaluation of the electrode materials using a Land battery tester (Land, Wuhan) at 1C, 3C, 1C/5C, 1C/10C and 1C/15C within the voltage range of 2.7-4.3 V. The cells were also tested at rates of, 0.2 C, 0.5 C, 1.0 C, 2.0 C, 5.0 C, 10 C and 15 C then at a rate of 0.2 C to analyze the rate capability. Cycling performance of NM90 and HE-Lu within (h) 2.7-4.5V (i) 2.7-4.6V (j) 2.7-4.7V. Additionally, cyclic voltammetry (CV) and electrochemical impedance spectroscopy (EIS) were conducted using a CHI760E electrochemical analyzer (Chenhua Instrument Co., Ltd., Shanghai). CV was recorded at different scan rates (0.1-0.5 mV s^{-1}) in the voltage range of 2.7-4.3 V. EIS was performed on a dual-electrode cell with a potential amplitude of 5 mV over a frequency range of 100 kHz to 0.01 Hz. EIS measurements of different samples at the 5th, 100th, and 200th cycles were conducted at a charging state of 4.0 V using an electrochemical workstation. The in-situ DRT test based on the in-situ EIS test was conducted at the 5th, 100th, and 200th cycle in the charging process at 3.7 V-4.3 V to test the EIS data at different SOC. The kinetic behavior was investigated using the galvanostatic intermittent titration technique

(GITT), with each charge/discharge time and resting time of 10 and 30 minutes, respectively. The rate of charging and discharging was 0.1C.

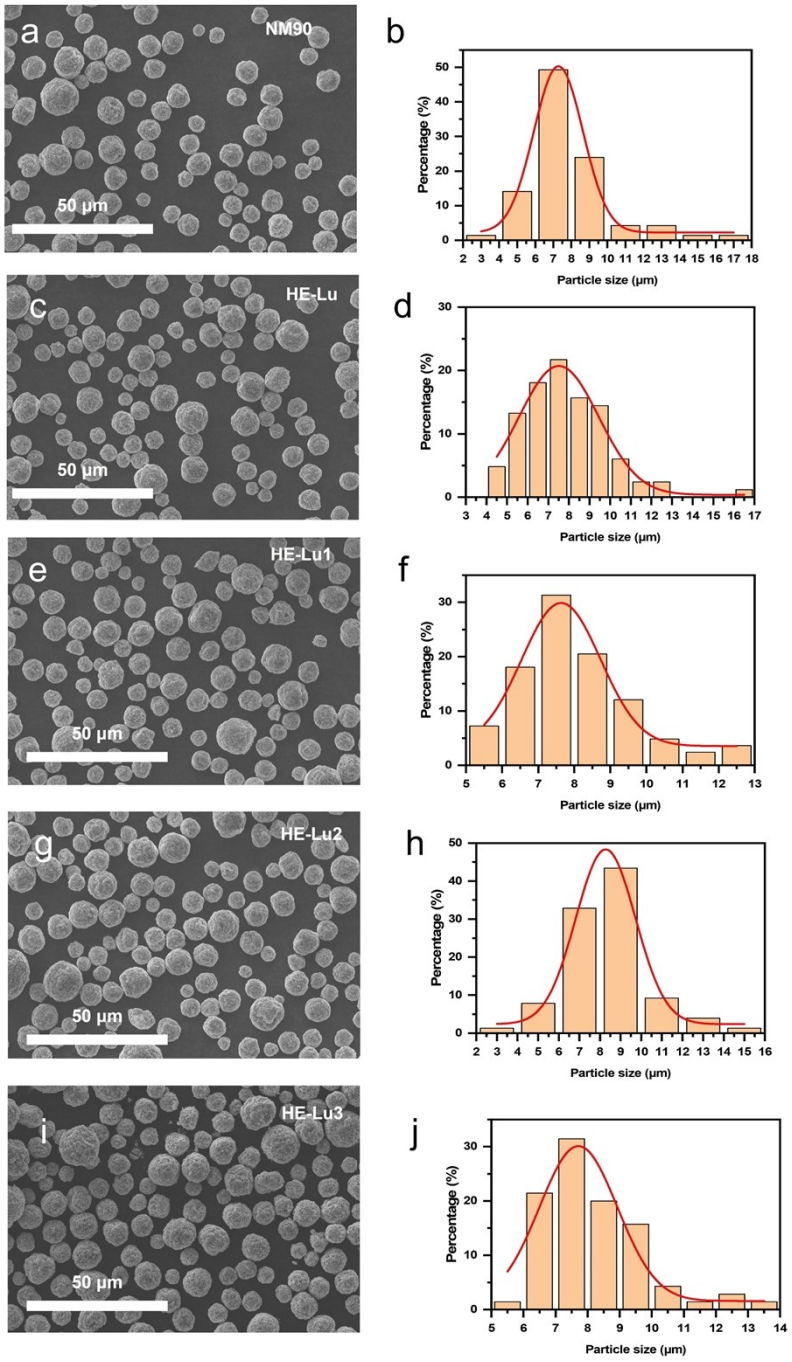

Figure S1. SEM images of precursors and the corresponding particle size distribution of (a, b) NM90, (c, d) HE-Lu, (e, f) HE-Lu1, (g, h) HE-Lu2, (i, j) HE-Lu3.

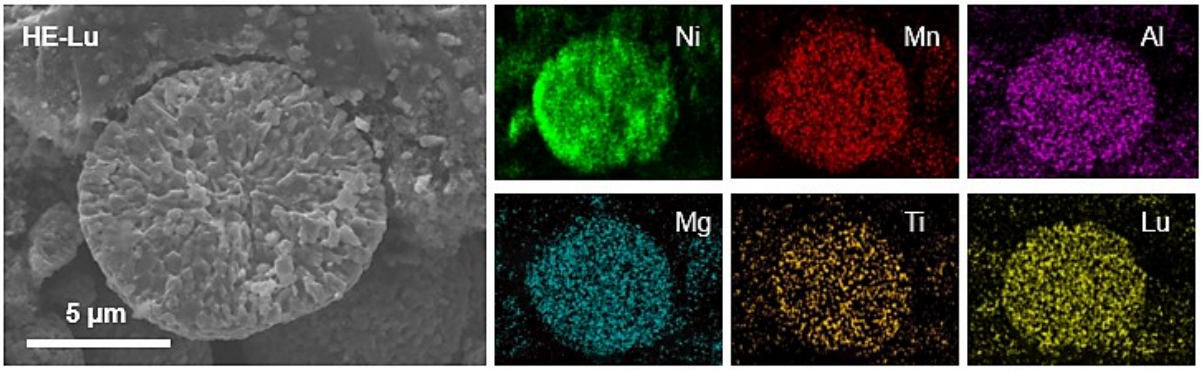

Figure S2. Cross-sectional SEM images and corresponding EDS mapping images of the HE-Lu.

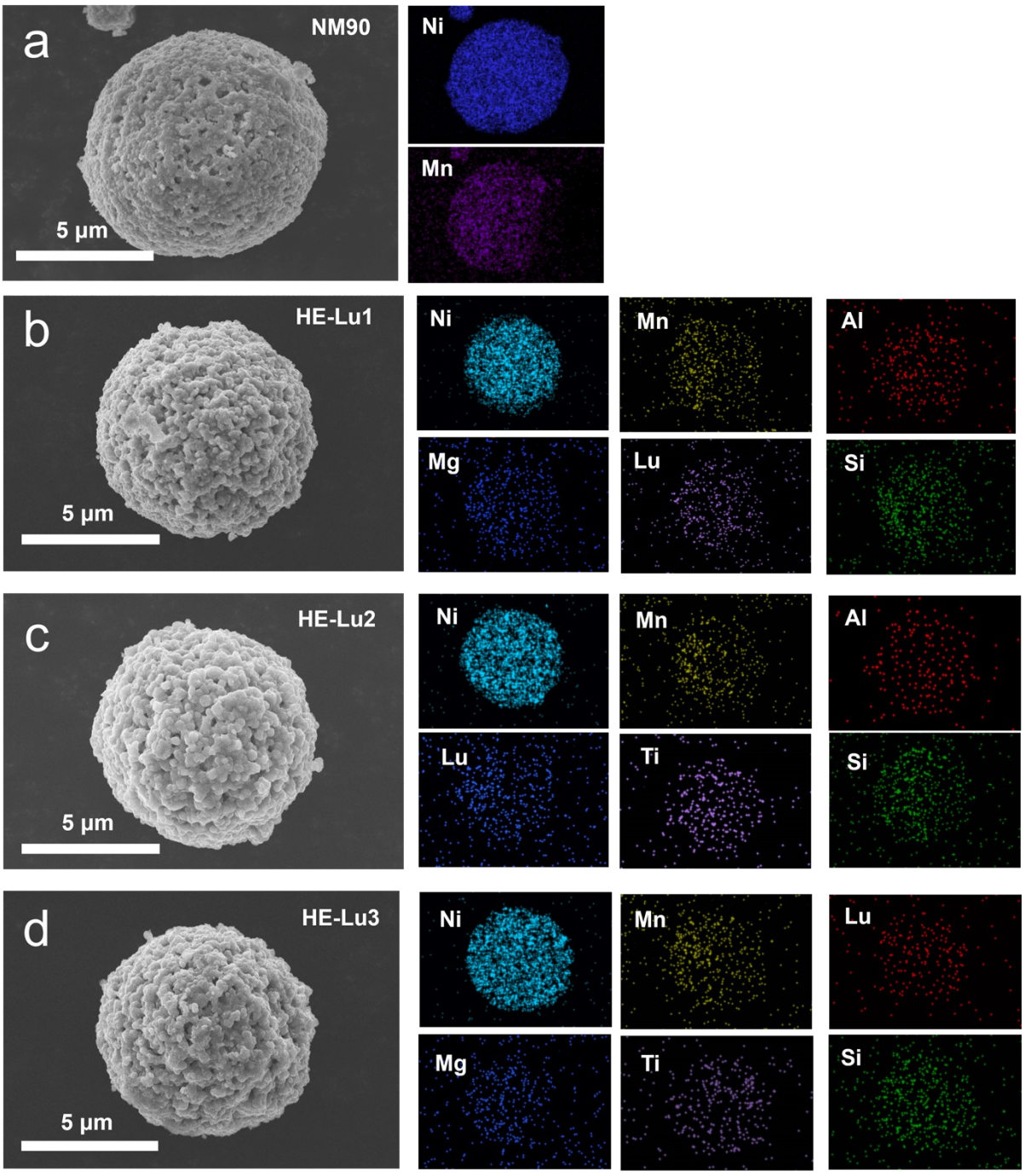

Figure S3. The SEM image and corresponding EDS mapping images of the (a) NM90, (b) HE-Lu1, (c) HE-Lu2, (d) HE-Lu3.

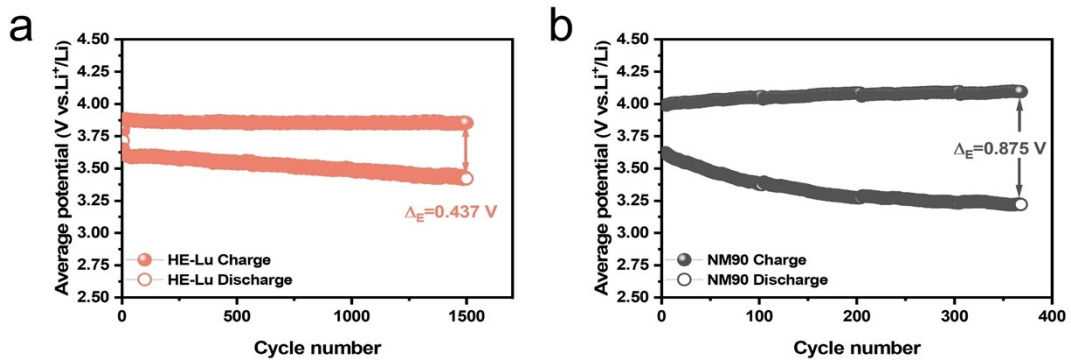

Figure S4. Average charge and discharge potential of (a) HE-Lu, (b) NM90.

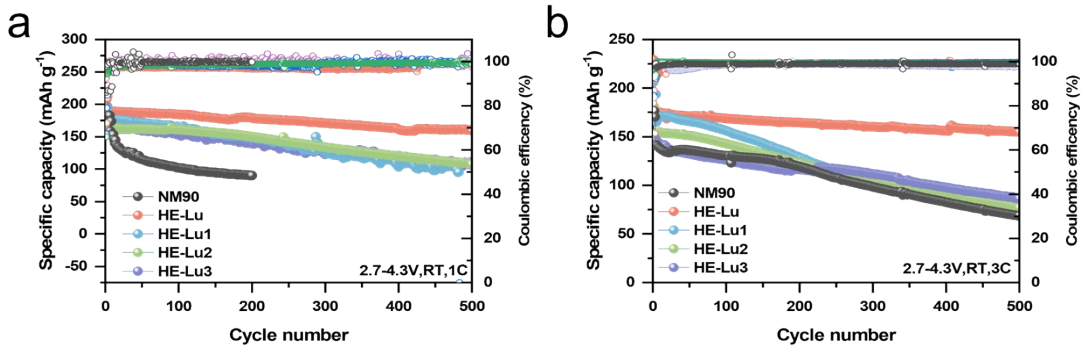

Figure S5. Long-term cycling stability of NM90, HE-Lu, HE-Lu1, HE-Lu2 and HE-Lu3 at (a) 1C and (b) 3C at RT.

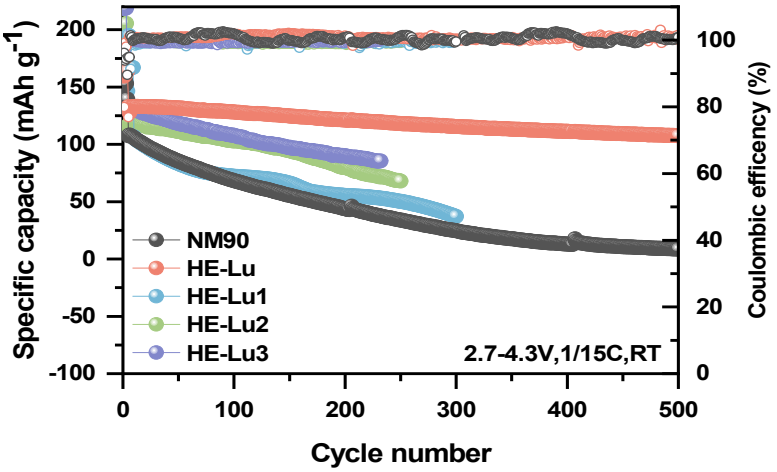

Figure S6. Long-term cycling stability of NM90, HE-Lu, HE-Lu1, HE-Lu2 and HE-Lu3 at 1/15C at RT.

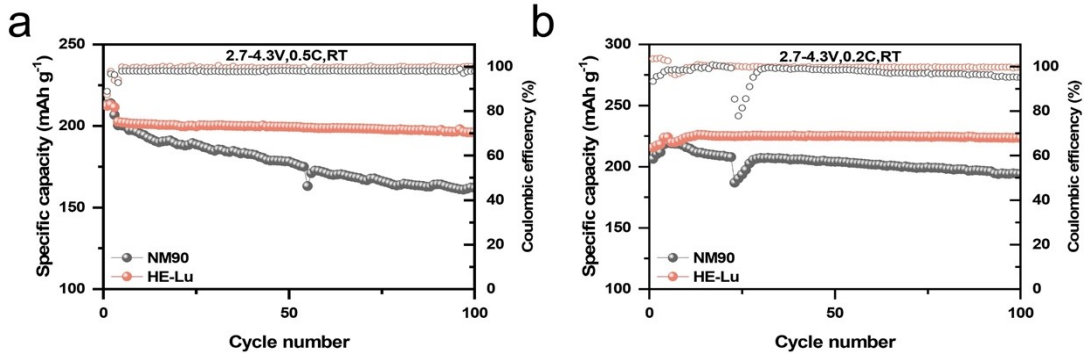

Figure S7. Long-term cycling stability of NM90 and HE-Lu at (a) 0.5C and (b) 0.2C at RT.

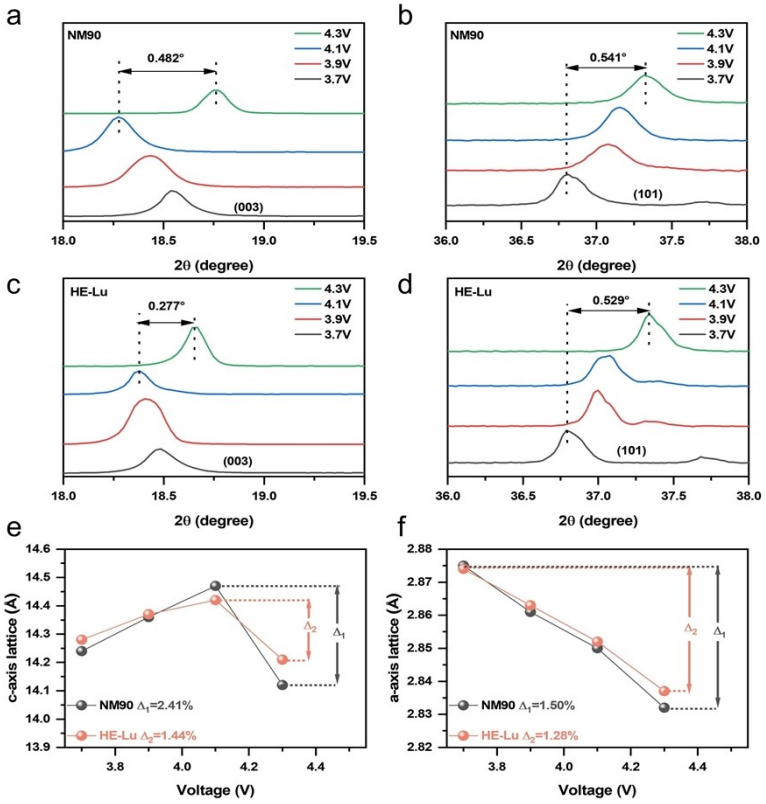

Figure S8. Ex-situ XRD of (a) peak (003) and (b) peak (101) of NM90 during initial charge and discharge at 0.1C. Ex-situ XRD of (c) peak (003) and (d) peak (101) of HE-Lu during initial charge and discharge at 0.1C. Lattice variations of (e) c-axis and (f) a-axis during charge and discharge for NM90 and HE-Lu.

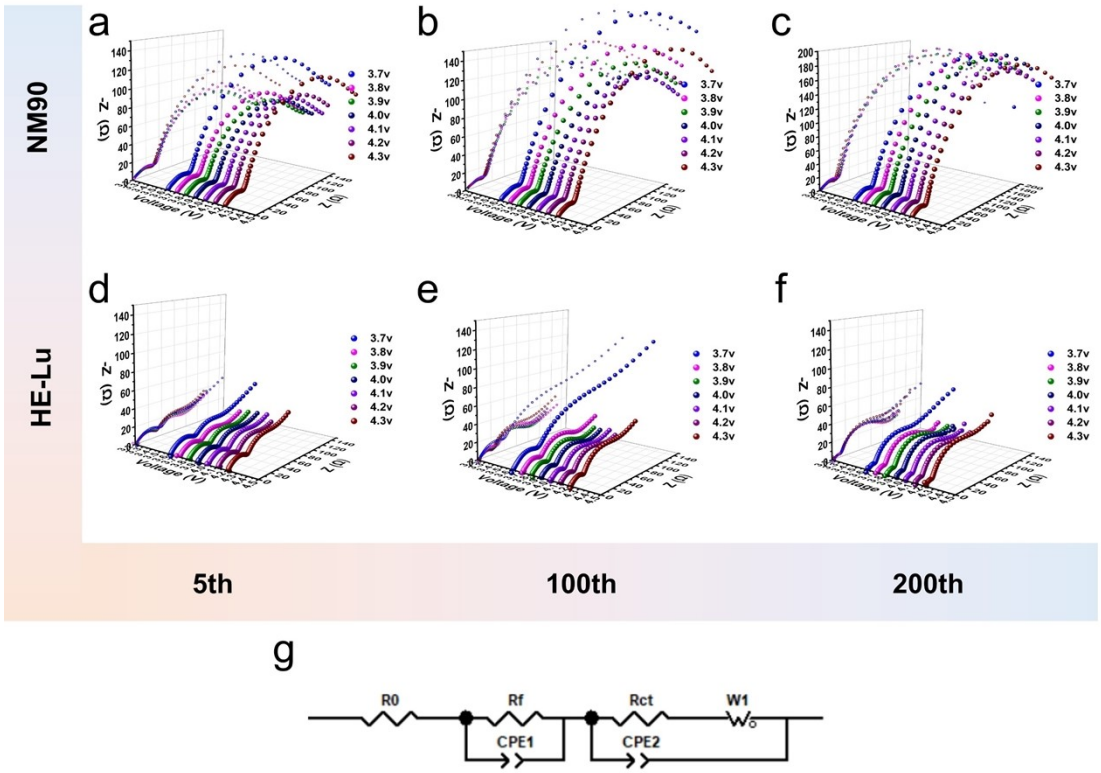

Figure S9. Nyquist plots of the impedance at 1C/5C for (a, b, c) NM90 and (d, e, f) HE-Lu. (g) Equivalent circuit model utilized to fit the EIS plots.

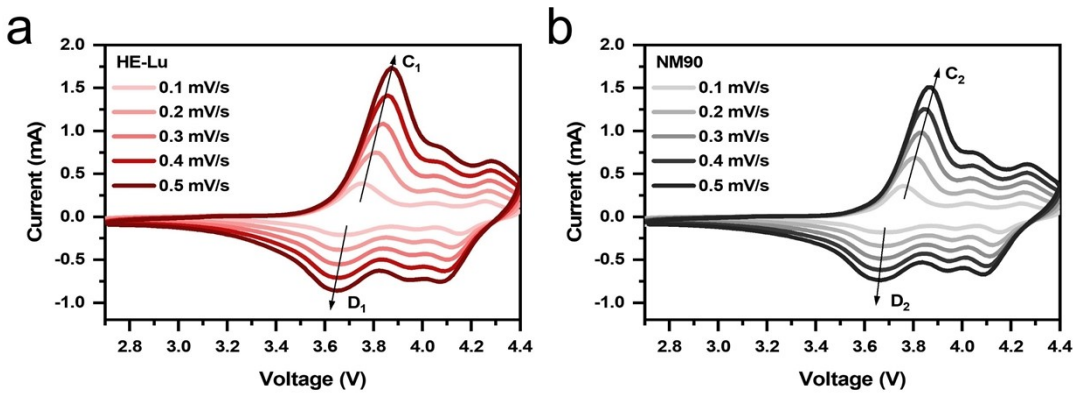

Figure S10. Cyclic voltammetry characterization of (a) HE-Lu and (b) NM90.

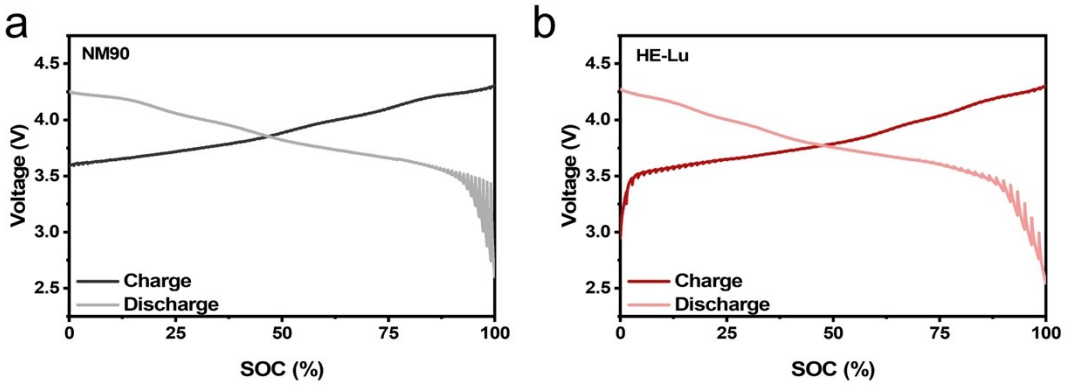

Figure S11. The GITT curves of (a) NM90 and (b) HE-Lu.

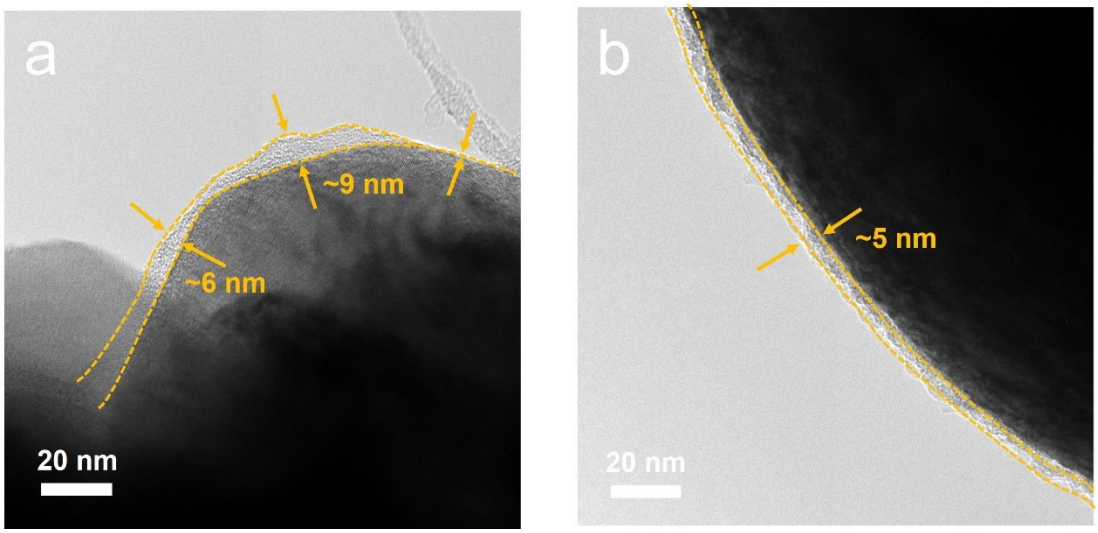

Figure S12. TEM image of (a) NM90 and (b) HE-Lu.

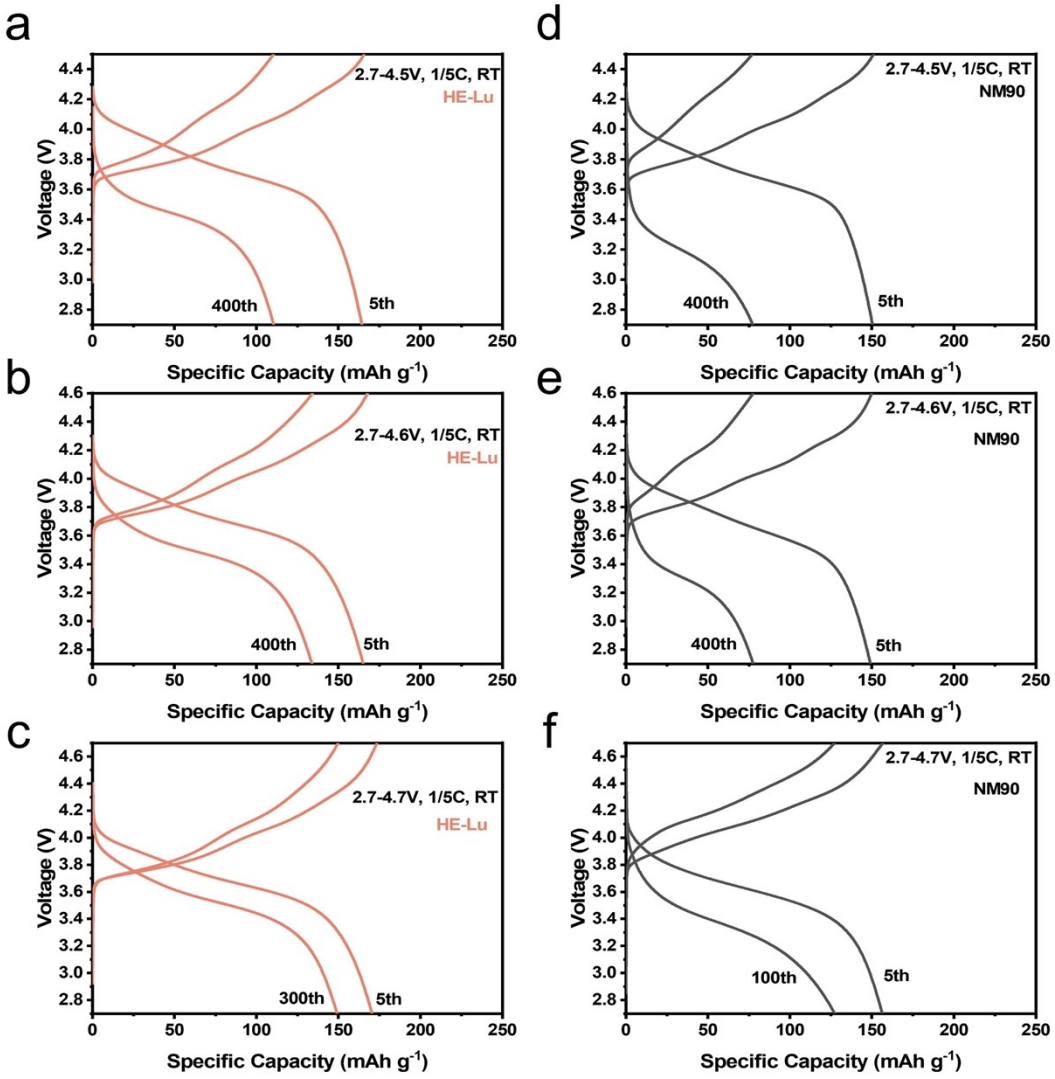

Figure S13. Charge–discharge curves of HE-Lu at (a) 2.7-4.5 V, (b) 2.7-4.6 V, (c) 2.7-4.7 V. Charge–discharge curves of NM90 at (d) 2.7-4.5 V, (e) 2.7-4.6 V, (f) 2.7-4.7 V.

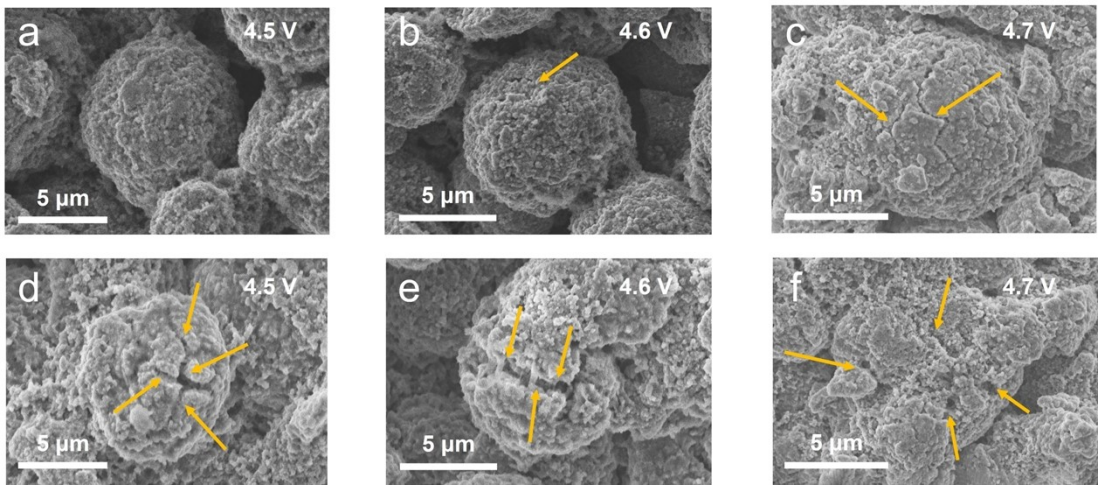

Figure S14. SEM images of HE-Lu after 200 cycles at 1C/5C within (a) 2.7-4.5 V, (b) 2.7-4.6 V, (c) 2.7-4.7 V. SEM images of NM90 after 200 cycles at 1C/5C within (d) 2.7-4.5 V, (e) 2.7-4.6 V, (f) 2.7-4.7 V.

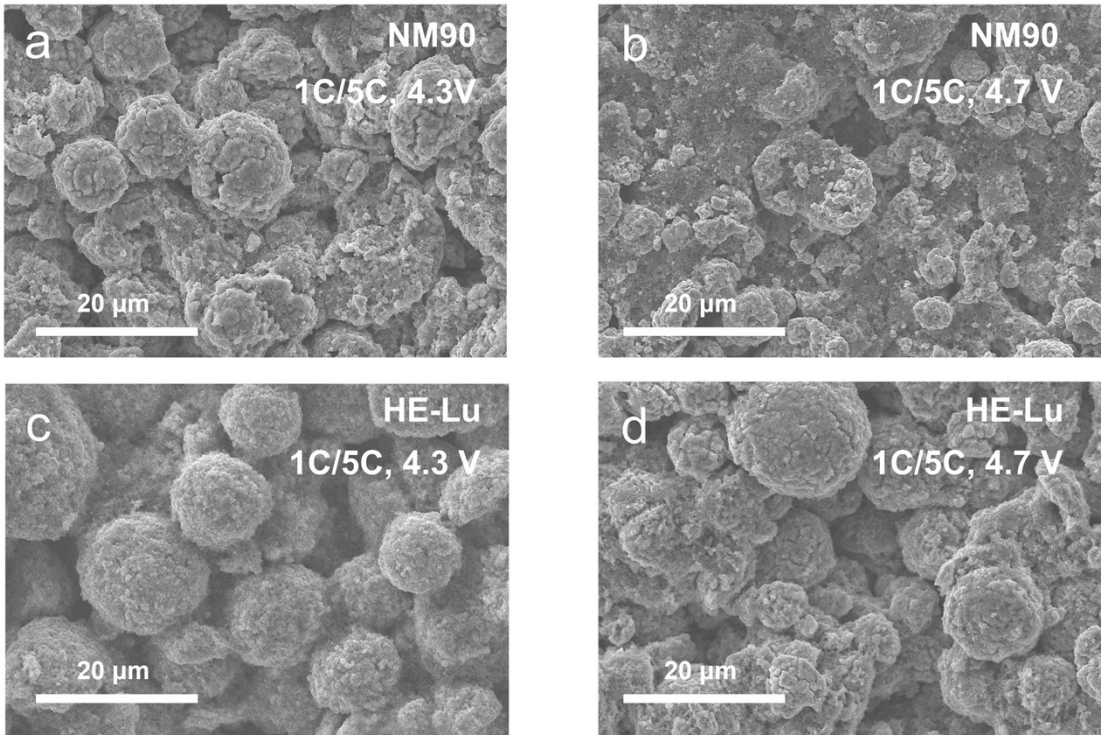

Figure S15. (a) SEM images of NM90 after 200 cycles at 1C/5C within 2.7-4.3 V. (b) SEM images of NM90 after 200 cycles at 1C/5C within 2.7-4.7 V. (c) SEM images of HE-Lu after 200 cycles at 1C/5C within 2.7-4.3 V. (d) SEM images of HE-Lu after 200 cycles at 1C/5C within 2.7-4.7 V.

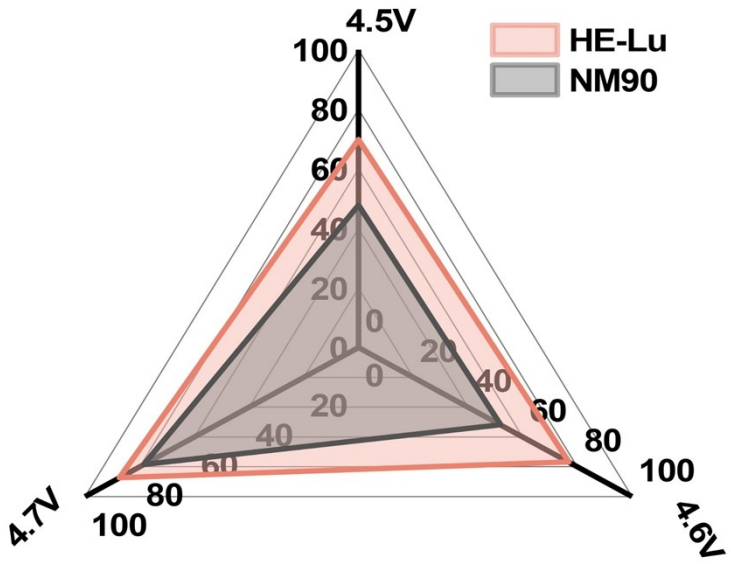

Figure S16. The capacity retention of NM90 and HE-Lu at high cut-off voltage through radar chart.

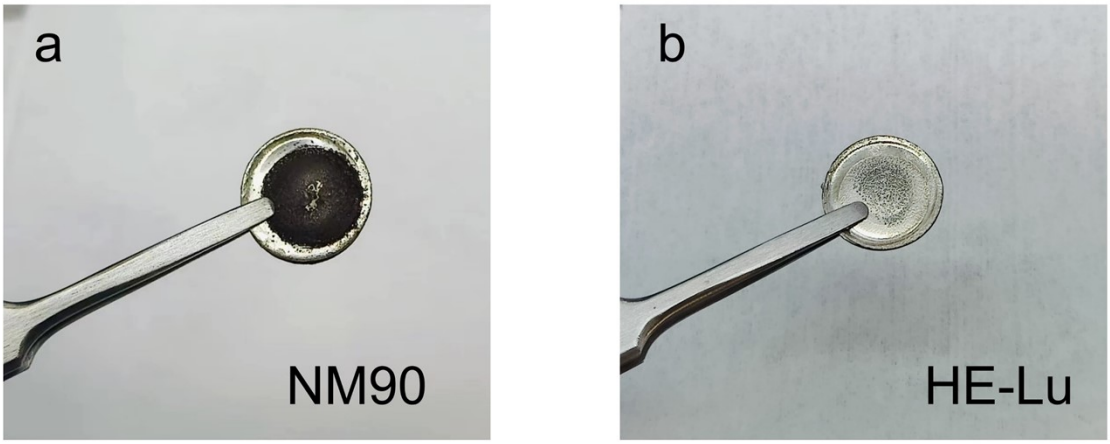

Figure S17. The photograph of the lithium anode after 200 cycles for (a) NM90 and (b) HE-Lu.

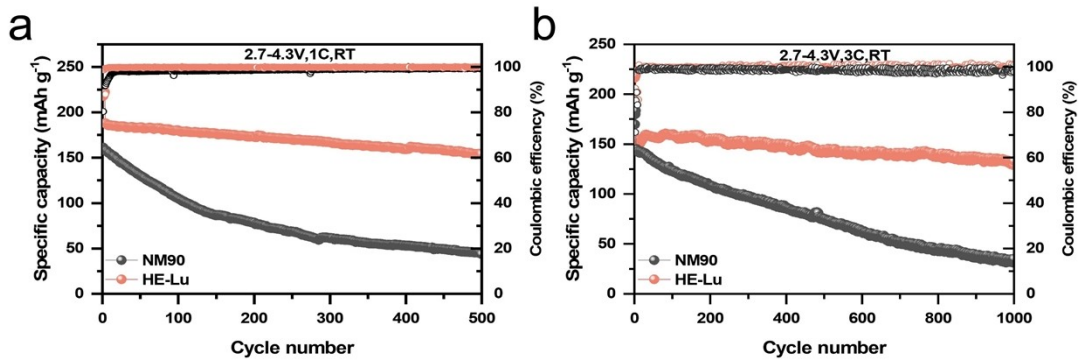

Figure S18. Cycling stability of NM90 and HE-Lu in full cells at (a) 1 C and (b) 3C.

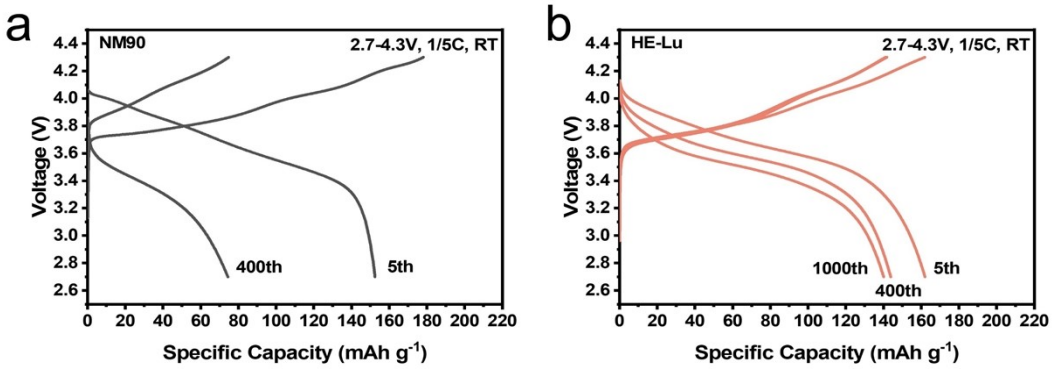

Figure S19. Charge–discharge curves of (a) NM90 and (b) HE-Lu at different cycles.

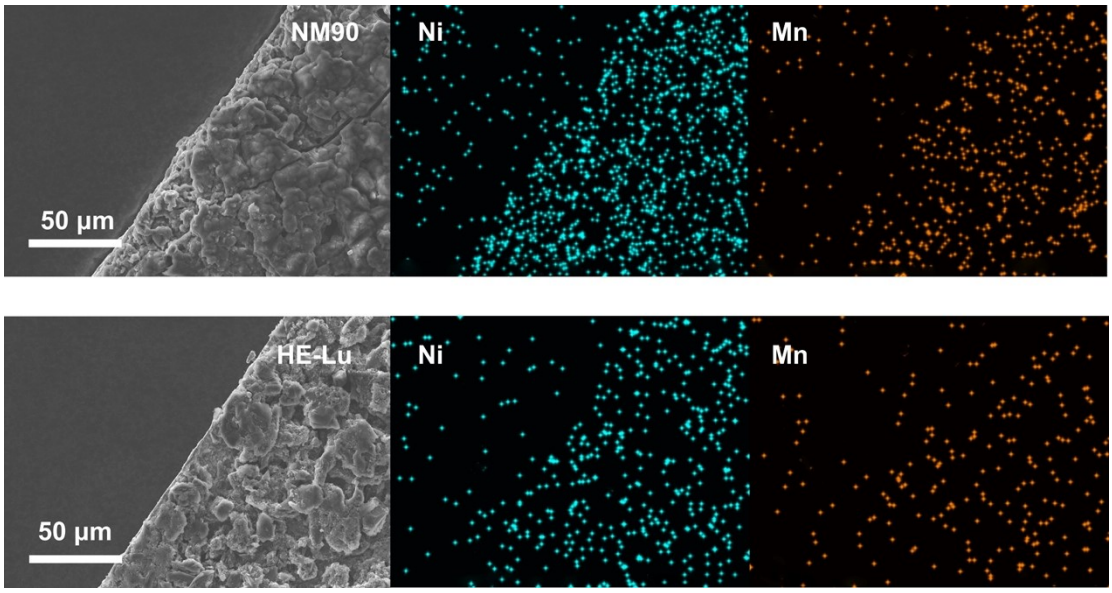

Figure S20. SEM images of graphite anode and EDS mapping of Ni and Mn after 200 cycles in full cell.

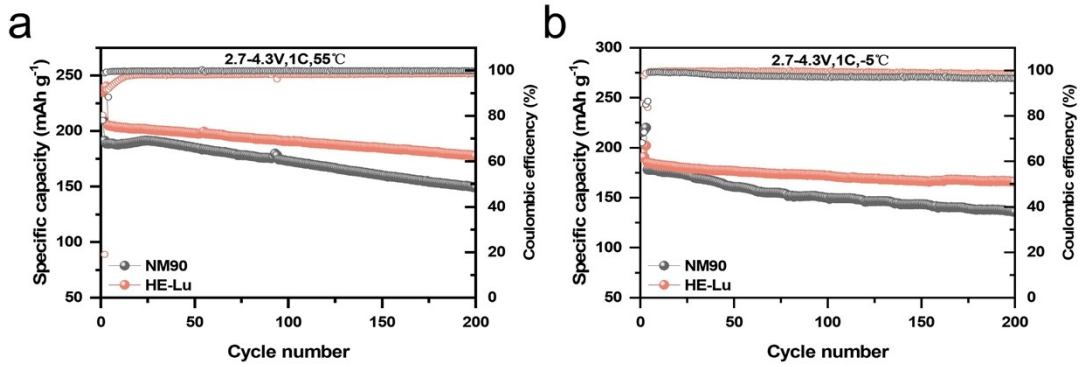

Figure S21. Long-term cycling stability of NM90 and HE-Lu in full cells at (a) 1C (55 °C) and (b) 1C (-5 °C).

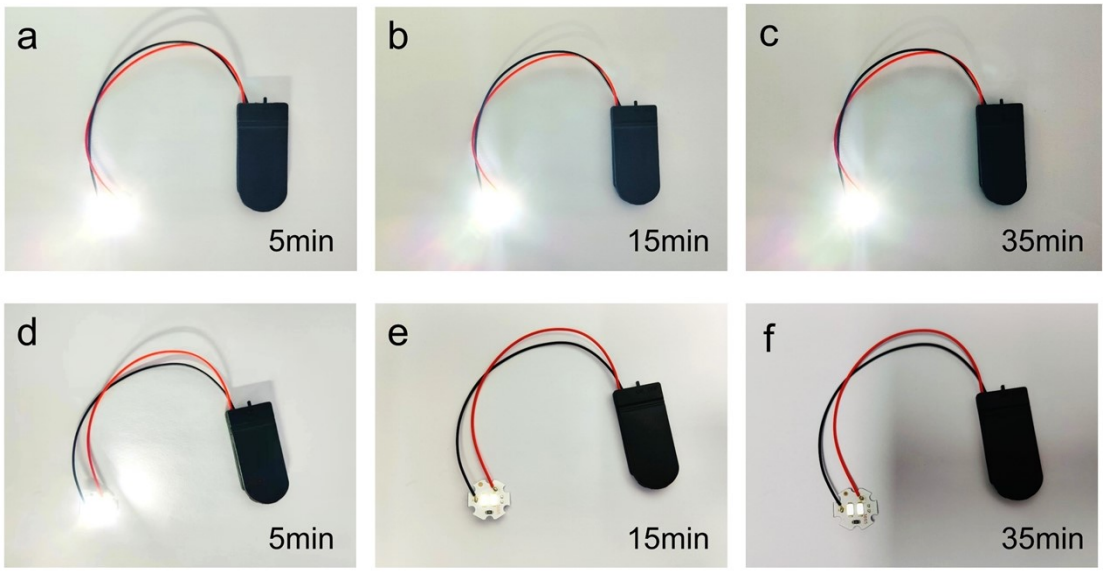

Figure S22. Long cycle life of (a-c) HE-Lu and (d-f) NM90 full cells in electronic devices.

Table S1. Chemical compositions of NM90 and HE-Lu.

Sample	Chemical composition (at. %)					
	Ni	Mn	Al	Mg	Ti	Lu
NM90	90.22	9.78	-	-	-	-
HE-Lu	90.07	2.04	1.97	1.99	2.04	1.89

Table S2. Cell parameters and statistics obtained from Rietveld refinement on the powder XRD patterns of NAM90 and HE-Lu.

Samples	NM90	HE-Lu
a-axis (Å)	2.8732	2.8746
c-axis (Å)	14.2147	14.2535
Volume ($Å^3$)	101.622	101.998
Ni^{2+} in Li site (%)	4.32%	2.39%
$I_{(003)}/I_{(104)}$	1.72	1.54
R_{wp} (%)	5.32%	6.79%

Table S3. The values of resistances of cathode electrolyte interphase (R_{CEI}) and charge transfer (R_{ct}), for the NM90 and HE-Lu after different cycles.

Materials	Cycle	R (Ω)	Voltage (V)							
			3.6	3.7	3. 8	3.9	4.0	4.1	4.2	4.3
NM90	5th	R_{CEI}	51.15	52.59	47.9	45.32	45.82	43.42	42.99	38.7
		R_{ct}	323.7	229.5	215.8	215.3	221.1	232.5	279.1	380.1
	100th	R_{CEI}	57.57	56.26	48.85	47.96	44.95	44.95	41.06	38.59
		R_{ct}	501.5	394.3	341.2	314.5	302.9	317.9	377	538.1
	200th	R_{CEI}	53.43	57.39	53.48	53.05	45.82	43.89	39.4	38.86
		R_{ct}	452.3	465.2	436.3	463.8	423.5	406.5	433.4	594.6
HE-Lu	5th	R_{CEI}	45.64	37.87	37.67	36.4	37.4	37.7	38.02	35.97
		R_{ct}	101.8	68.12	73.9	77.19	76.19	78.09	92.81	98.67
	100th	R_{CEI}	54.68	37.56	33.2	29.12	26.54	25.9	26.47	27.27
		R_{ct}	263.5	88.52	74.52	74.45	75.22	78.22	93.58	102.34
	200th	R_{CEI}	19.06	22.97	24.7	22.33	20.1	19.43	20.22	18.84
		R_{ct}	94.07	113.5	88.51	90.01	89.18	90.57	107.7	107.2

Table S4. Comparisons of the electrochemical performances between this work and the reported Ni-rich cathodes.

Cathode composition	Voltage range (V)	Temp. (°C)	1st discharge capacity (mAh g^{-1}/C)	Cycling stability	Cell type	Ref.
$LiNi_{0.9}Mn_{0.02}Al_{0.02}Mg_{0.02}Ti_{0.02}Lu_{0.02}O_2$	**2.7-4.3**	**RT**	**195.8 (1C)**	**83.1% (1C, 500 cycles)**	**Half cells**	**This work**
	2.7-4.3		**177.1 (3C)**	**90.6% (3C, 500 cycles)**		
	2.7-4.3		**161.9 (1C/5C)**	**84.1% (1C/5C, 1500 cycles)**		
	2.7-4.3		**137.6 (1C/10)**	**74.4% (1C/10, 1500 cycles)**		
	2.7-4.3		**149.7 (1C/5C)**	**88.3% (1C/5C, 1000 cycles)**	**Full cells**	
	2.7-4.3		**139.2 (1C/10C)**	**71.3% (1C/10C, 1000 cycles)**		
	2.7-4.3		**132.9 (1C/15C)**	**81.9% (1C/15C, 500 cycles)**	**Half cells**	
	2.7-4.5		**155.7 (1C/5C)**	**69.8% (1C/5C, 400 cycles)**		
	2.7-4.6		**158.2 (1C/5C)**	**76.8% (1C/5C, 400 cycles)**		
	2.7-4.7		**164.3 (1C/5C)**	**87.4% (1C/5C, 300 cycles)**		
Mo-doped $LiNi_{0.9}Mn_{0.1}O_2$	3.0-4.3	RT	192 (1C)	85.6% (1C, 1000 cycles)	Full cells	[1]
Co-coated $LiNi_{0.91}Mn_{0.03}Co_{0.06}O_2$	3.0-4.3	RT	202 (0.5C)	87% (0.5C, 100 cycles)	Half cells	[2]
SO_2-treated $LiNi_{0.91}Co_{0.06}Mn_{0.03}O_2$	3.0-4.3	RT	180 (1C)	91% (1C, 100 cycles)	Half cells	[3]
Aaminosiloxane-coated $LiNi_{0.9}Co_{0.1}O_2$	2.8-4.35	RT	194.9 (1C)	77.2% (1C, 300 cycles)	Half cells	[4]
$LiNi_{0.93}Al_{0.05}Ti_{0.01}Mg_{0.01}O_2$	2.5-4.2	RT	190 (0.5C)	82% (0.5C, 800 cycles)	Full cells	[5]
Sr -doped $LiNi_{0.83}Co_{0.11}Mn_{0.06}O_2$	2.7-4.3	RT	195(1C)	90.1% (1C, 150 cycles)	Half cells	[6]
Al/B co-doped $LiNi_{0.88}Co_{0.09}Mn_{0.03}O_2$	2.7-4.3	RT	199 (1.0C)	92.2% (1C, 100 cycles)	Half cells	[7]
PEDOT-coated $LiNi_{0.85}Co_{0.1}Mn_{0.05}O_2$	2.7-4.3	RT	177 (1C)	91% (1C, 100 cycles)	Half cells	[8]
$LiNi_{0.6}Mn_{0.2}Co_{0.2}O_2$	2.7-4.3	RT	145 (0.2C/4C)	96.5% (0.2C/4C, 160 cycles)	Half cells	[9]
B-doping $LiNi_xCo_yMn_zO_2$	3.0-4.4	RT	200 (1C)	91% (1C, 100 cycles)	Half	[10]

					cells	
$Li_xSn_yO_z$ coating $LiNi_{0.8}Co_{0.1}Mn_{0.1}O_2$	2.8-4.3	RT	194 (1C)	77% (1C, 200 cycles)	Half cells	[11]
$LiTi_{0.5}Zr_{1.5}(PO_4)_3$(LTZP) coating $LiNi_{0.8}Co_{0.1}Mn_{0.1}O_2$	2.7-4.3	RT	189 (1C)	84.7% (1C, 200 cycles)	Half cells	[12]
$LiNi_{0.83}Co_{0.11}Mn_{0.06}O_2$	3.0-4.3	RT	197 (0.5C)	87.9% (1C, 200 cycles)	Half cells	[13]
Al/Zr co-doped $LiNi_{0.88}Co_{0.09}Mn_{0.03}O_2$	2.75-4.3	RT	193 (0.5C)	93% (0.5C, 150 cycles)	Half cells	[14]
Li_4SiO_4 coating $LiNi_{0.8}Co_{0.15}Al_{0.05}O_2$	2.7-4.3	RT	213.2 (0.1C)	70.6% (10C, 300 cycles)	Half cells	[15]
B_2O_3 coating $LiNi_{1/3}Co_{1/3}Mn_{1/3}O_2$	3.0–4.5	RT	131.3 (1C)	86% (2C, 100 cycles)	Half cells	[16]
Agglomerated-NCM811	2.8–4.3	RT	203.7 (0.2C)	94.1% (5C, 100 cycles)	Half cells	[17]
Nanorod-like NCM622	2.8–4.4	RT	152.2 (5.0C)	90.6 % (5C, 200 cycles)	Half cells	[18]
$LiAlO_2$/ $Si_{1-x}Al_xO_2$ hybrid coating NCM622	2.7–4.5	RT	206.5 (0.1C)	78.6 % (5C, 500 cycles	Half cells	[19]
$LiNi_{0.5}Mn_{0.3}Co_{0.2}O_2$	2.75–4.2 V	RT	-	90 % (6C, 175 cycles)	Half cells	[20]
				90 % (10C, 80 cycles)	Half cells	

References

1. G.-T. Park, B. Namkoong, S.-B. Kim, J. Liu, C. S. Yoon and Y.-K. Sun, *Nat. Energy*, 2022, **7**, 946-954.
2. Y. Kim, H. Park, K. Shin, G. Henkelman, J. H. Warner and A. Manthiram, *Adv. Energy Mater.*, 2021, **11**, 2101112.
3. W. M. Seong, K.-H. Cho, J.-W. Park, H. Park, D. Eum, M. H. Lee, I.-s. S. Kim, J. Lim and K. Kang, *Angew. Chem. Int. Ed.*, 2020, **59**, 18662-18669.
4. R. Wang, J. Wang, S. Chen, Q. Yuan, D. Li, X. Zhang, L. Chen, Y. Su, G. Tan and F. Wu, *Nano Energy*, 2020, **76**, 105065.
5. Z. Cui, Q. Xie and A. Manthiram, *Adv. Energy Mater.*, 2021, **11**, 2102421.
6. L. Ni, H. Chen, W. Deng, B. Wang, J. Chen, Y. Mei, G. Zou, H. Hou, R. Guo, J. Xie and X. Ji, *Adv. Energy Mater.*, 2022, **12**, 2103757.
7. Y.-J. Guo, C.-H. Zhang, S. Xin, J.-L. Shi, W.-P. Wang, M. Fan, Y.-X. Chang, W.-H. He, E. Wang, Y.-G. Zou, X. a. Yang, F. Meng, Y.-Y. Zhang, Z.-Q. Lei, Y.-X. Yin and Y.-G. Guo, *Angew. Chem. Int. Ed.*, 2022, **61**, e202116865.
8. G.-L. Xu, Q. Liu, K. K. S. Lau, Y. Liu, X. Liu, H. Gao, X. Zhou, M. Zhuang, Y. Ren, J. Li, M. Shao, M. Ouyang, F. Pan, Z. Chen, K. Amine and G. Chen, *Nat. Energy*, 2019, **4**, 484-494.
9. S. Oh, A. R. Jeon, G. Lim, M. K. Cho, K. H. Chae, S. S. Sohn, M. Lee, S.-K. Jung and J. Hong, *Energy Storage Mater.*, 2024, **65**, 103169.
10. S. F. Amalraj, R. K. Raman, A. Chakraborty, N. Leifer, R. Nanda, S. Kunnikuruvan, T. Kravchuk, J. Grinblat, V. Ezersky, R. Sun, F. L. Deepak, C. Erk, X. Wu, S. Maiti, H. Sclar, G. Goobes, D. T. Major, M. Talianker, B. Markovsky and D. Aurbach, *Energy Storage Mater.*, 2021, **42**, 594-607.
11. A. Saha, O. Shalev, S. Maiti, L. Wang, S. H. Akella, B. Schmerling, S. Targin, M. Tkachev, X. Fan and M. Noked, *Mater. Today Energy*, 2023, **31**, 101207.
12. S. Luo, F. Yang, Z. Xiong, Y. Wu, X. Ao, C. Li, Q. Chen and K. Wang, *Chem. Eng. J.*, 2022, **448**, 137663.
13. X.-H. Meng, T. Lin, H. Mao, J.-L. Shi, H. Sheng, Y.-G. Zou, M. Fan, K. Jiang, R.-J. Xiao, D. Xiao, L. Gu, L.-J. Wan and Y.-G. Guo, *J. Am. Chem. Soc.*, 2022, **144**, 11338-11347.
14. X. Ou, T. Liu, W. Zhong, X. Fan, X. Guo, X. Huang, L. Cao, J. Hu, B. Zhang, Y. S. Chu, G. Hu, Z. Lin, M. Dahbi, J. Alami, K. Amine, C. Yang and J. Lu, *Nat. Commun.*, 2022, **13**, 2319.
15. J.-c. Zheng, Z. Yang, Z.-j. He, H. Tong, W.-j. Yu and J.-f. Zhang, *Nano Energy*, 2018, **53**, 613-621.
16. J. Li, Z. Liu, Y. Wang and R. Wang, *J. Alloys Compd.*, 2020, **834**, 155150.
17. Y. Zhang, K. Du, Y. Cao, Y. Lu, Z. Peng, J. Fan, L. Li, Z. Xue, H. Su and G. Hu, *J. Power Sources*, 2020, **477**, 228701.
18. F. Li, Z. Liu, J. Shen, X. Xu, L. Zeng, B. Zhang, H. Zhu, Q. Liu, J. Liu and M. Zhu, *J. Mater. Chem. A*, 2021, **9**, 2830-2839.
19. H. Wang, Y. Chu, Q. Pan, C. Tan, Y. Shi, Y. Li, S. Hu, F. Zheng, Y. Huang and Q. Li, *ACS Sustainable Chem. Eng.*, 2021, **9**, 8951-8961.
20. D. Ouyang, B. Liu, J. Huang and Z. Wang, *Process Saf. Environ. Prot.*, 2024, **185**, 76-85.